State space model of an array of oscillating water column wave energy converters with inter-body hydrodynamic coupling

D.T. Gaebele [a,*], M.E. Magaña [a], T.K.A. Brekken [a], O. Sawodny [b]

[a] Electrical Engineering and Computer Science (EECS), Oregon State University, OR 97331, USA
[b] Institute for System Dynamics, University of Stuttgart, Stuttgart, Baden-Württemberg 70550, Germany

ARTICLE INFO

ABSTRACT

In this paper we derive a state-space model restricted to heave motion of a full scale array of floating oscillating-water-column (OWC) wave energy converters with nonlinear power take off dynamics, taking hydrodynamic interactions between all bodies into account. The resulting state-space model is intended as a basis for accelerated development of advanced control approaches to maximize power generation. The kinetic and potential energy transferred to the air chamber causes a pressure difference, inducing unidirectional motion of a novel bi-radial turbine. This can be accurately modeled using pressure dependent turbine characteristics, taking into account the nonlinearity of the gas compressibility. The analytical model of the floating OWC is based on linear hydrodynamic coefficients, obtained using the boundary element solver ANSYS Aqwa of an equilateral triangle array of axis-symmetric floating OWCs of the Marmok-A-5 type. Finally, the system's model time domain equations are simulated in different wave climates and an ideal active controller is applied to maximize energy conversion. For the specific implemented separation distance the resulting cross body interactions are found to be negligible in irregular compared to regular wave scenarios. The turbine rotational speed suggests investigations on discontinues nonlinear control methods before semi-global approaches are used to optimize power generation.

1. Introduction

Wave energy is a promising renewable energy source and potentially contributes significantly to the future energy mix (Aderinto and Li, 2018). Thus, research in this field has increased substantially over the last decade (Falcão, 2010) and in the recent past more single prototypes and operational sites have been deployed (Rusu and Onea, 2017). However, significant costs associated with development and maintenance have so far impeded the implementation of commercially viable projects (Andrews and Jelley, 2017). To achieve commercial power generation in the future wave energy converters (WECs) will be deployed in large WEC farms (Chowdhury et al., 2015). The spacing between single devices is on the one hand determined by a trade off between safe maintenance operation and cost reduction due to shorter cables for power transmission and on the other hand by the benefits for power generation. Depending on the configuration of the array the produced power can be higher or lower compared to the same amount of isolated devices, due to hydrodynamic interactions between the ocean waves and those radiated by the WECs (Chowdhury et al., 2015; Budal,

1977; Falcão, 2002; Nader et al., 2014). Bodies immersed in water will experience additional effects apart from buoyancy if surrounded by an unsteady flow, due to the pressure the water acts on them. This can set the body into motion, resulting in a subsequent motion of the surrounding water thus some of the bodies' kinetic energy is radiated away. However, a second body in the array configuration can experience this radiated wave as an additional incident wave (Falnes, 2002). Those interactions vary for differently shaped devices, locations and incident wave directions consequently those interactions are non trivial to derive analytically (Sabuncu and Calisal, 1981) or to test experimentally for scaled prototypes in wave tanks (Nader et al., 2017). Today it is common practice to assess the main hydrodynamic coefficients using the boundary element method (BEM) to solve the velocity potential of the flow, followed by a transformation in the time domain, which is necessary if nonlinear effects want to be considered in the model (Sheng et al., 2014). Additionally, the power generated in a scaled physical model does not scale linearly to its size (Henriques et al., 2016b). Hence, it is advantageous to use a detailed full-scale mathematical model to predict the power generation capabilities as

---

done in Forehand et al. (2016) with a single-body point absorber array. Furthermore, the model can be used to design control strategies at an early stage. In Bacelli and Ringwood (2015) the authors present an optimal control approach of WEC array for single and multibody devices with linear velocity power take off (PTO) relation and linear dynamics. A strategy taking into account hydrodynamic interactions while solving the control problem is introduced in Nambiar et al. (2015) for three hemispherical floats connected to a fixed support with a rigid arm. To this date the authors do not know of any studies addressing optimal control of multibody systems with nonlinear PTO, taking the hydrodynamics into account. Consequently, our current work addresses the necessary modeling aspects, validated based on a given control law and our future work will address new control strategies in order to optimize the energy conversion of large parks of WECs. This paper deals with wave energy converters of the floating oscillating water column type (OWC) illustrated in Fig. 1. The basics of the principle is an off-shore device open to the sea water at the bottom and a trapped air chamber. In general OWCs are considered as one of the simplest WECs, since they have few moving mechanical parts and the PTO has no water contact, sealing the air chamber to the atmosphere (Falcão and Henriques, 2016). The oscillating motion of the water column with the waves induces an alternating air flow, thus so-called self-rectifying turbines are installed in OWCs to achieve a unidirectional rotation. Apart from the well studied Well's turbine, impulse turbines are another class of axial flow machines. A new impulse turbine, the bi-radial turbine (see Fig. 2) is a good choice in terms of performance, with a peak efficiency of 79% (Falcão and Henriques, 2016), thus we use the dynamic model of this turbine from Henriques et al. (2017a) and Henriques et al. (2017) for the implementation of an OWC array in this work. The air flow into the rotor is directed through so called guide vanes. There are two distinct connected rows of guide vanes, illustrated in blue. By sliding the complete guide vanes set axially, it will be inserted into or removed from the flow to ensure that the downstream guide vanes do not obstruct the flow out of the rotor. Additionally a high speed stop valve (HSSV) is installed at the bottom of the turbine, to prevent water contact in extreme sea states by stopping the entire air flow. The description of these analytical relationships is followed by a numerical simulation of the hydrodynamic coefficients for the specifically used geometries, with the aid of the boundary element method solver (ANSYS Aqwa). Subsequently, the implementation that puts together the analytical and numerical parts is presented and the resulting simulation model is validated based on regular and irregular sea states. This work is concluded with a discussion of possible control approaches to improve power generation.

2. System modeling

The following model is based on linear water wave theory, assuming small wave amplitudes and body motions compared to the wave length λ. Additionally, the diameter of the inner tube is $d_p \ll \lambda$, justifying the internal free surface representation by an imaginary rigid piston, enabling the application of oscillating body theory between the OWC (indicated by d_p) and the floater (indicated by d_b from buoy). This will be called a two-body heaving system (Falnes, 2002). The terms piston and OWC are used interchangeably throughout the paper. The main axis of motion useful for power generation of the floating OWC is the heave axis, thus our research focuses on the dynamics of the vertical displacement $z(t)$, positive in the upwards direction.

2.1. Equations of motion

Let us assume we have an array on N WEC devices, leading to $2N$ coupled bodies. The equations of motion (EOM) for a body i oscillating in heave in the ocean after Cummins approach (Cummins, 1962) are given by

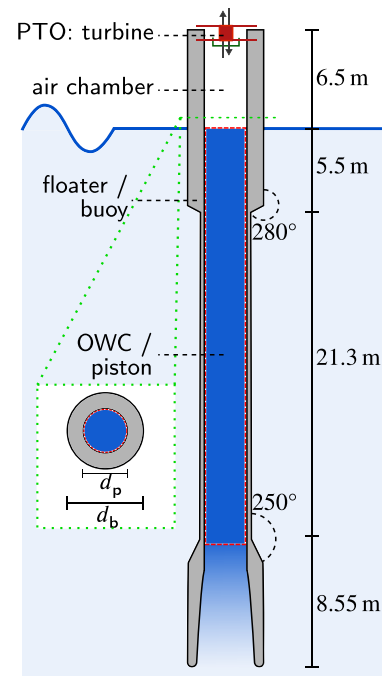$$m_i \ddot{z}_i(t) = F_i^H(t) + F_i^M(t) + F_i^{PTO}(t) + F_i^{Ex}(t) + F_i^R(t), \qquad (1)$$

Fig. 1. Conceptual sketch of a floating OWC with one equipped turbine. The OWC surrounded by the dashed line represents the piston.
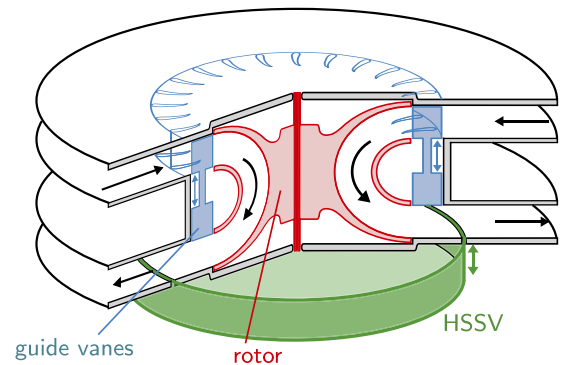

Fig. 2. Sketch of the bi-radial turbine.
Source: Adapted from Henriques et al. (2016b).

Here m_i denotes the mass of the individual body. The hydro-static restoring force

$$F_i^H(t) = \begin{cases} -\rho g S_b z_i(t), & \text{for a buoy} \\ -\rho g S_p z_i(t), & \text{for a piston} \end{cases}, \qquad (2)$$

due to the displaced water is zero at equilibrium $z_i(t) = 0$ and else adds a spring like effect to the system. S_b, S_p are the constant cross sections of a buoy, or a piston, ρ the sea water density and g the earth acceleration. The mooring force F_i^M is subject to the used mooring configuration, which will be attached to the buoys and will be simplified to a function of the heave position, hence

$$F_i^M(t) = \begin{cases} -f(z_i(t)), & \text{for a buoy} \\ 0, & \text{for a piston} \end{cases}. \qquad (3)$$

In the equation of the hypothetical piston F^M does not appear, since the OWC is not affected by the mooring. The forced induced by the relative motion in the two-body heaving system results in a varying pressure inside the air chamber $p_i(t)$. The pressure difference to the

atmosphere $p_i(t) - p_{at}$ acts as a force in opposite direction on the buoy and piston (Henriques et al., 2017a), namely,

$$F_i^{PTO}(t) = \begin{cases} (p_i(t) - p_{at})S_p, & \text{for a buoy} \\ -(p_i(t) - p_{at})S_p, & \text{for a piston} \end{cases}. \tag{4}$$

Additionally the change rate of the pressure is determined by the power take off (PTO) dynamics, by means of the air flow through the turbine and consequently the generator torque. Our control inputs will act over this force to our system (see 2.2). The local wave-induced excitation force is obtained as a superposition of N_w wave components (Henriques et al., 2017a)

$$F_i^{Ex}(t) = \sum_{k=1}^{N_w} \Gamma_i(\omega_k, \theta) A_k \cos(\omega_k t + \phi_k + \Phi_i(\omega_k, \theta)). \tag{5}$$

Here ϕ_k is the phase of each component and is a uniformly distributed random variable in the range $[0, 2\pi]$, which yields an irregular wave. The hydrodynamic excitation coefficient $\Gamma_i(\omega_k, \theta)$ at the wave frequency ω_k will strongly vary for different WECs, since it is dependent on the array configuration and the resulting diffraction of the incident wave field with the incident wave angle θ, commonly known as the diffraction problem. The corresponding phase component to $\Gamma_i(\omega_k, \theta)$ is denoted by $\Phi_i(\omega_k, \theta)$. The amplitudes of the waves A_k depend on the used wave spectrum $S_\omega(\omega)$. The hydrodynamic interactions due to the radiation problem are taken into account with the force

$$F_i^R(t) = \underbrace{\sum_{j=1}^{2N} A_{ij}^\infty \ddot{z}_j}_{F_i^{R,\infty}} - \underbrace{\sum_{j=1}^{2N} \int_0^t K_{ij}(t-\tau)\dot{z}_j(\tau)d\tau}_{F_i^{R'}}, \tag{6}$$

acting on body i due to body j. In consideration of the state space representation, the radiation force will be separated into a component $F_i^{R,\infty}$ due to the explicit dependence on the acceleration $\ddot{z}_j(t)$ and $F_i^{R'}$ due to the explicit dependence on the velocity $\dot{z}_j(t)$ of the jth body. This representation of the radiating phenomenon makes use of the linear hydrodynamic coefficients A_{ij}^∞, the constant added mass on body i due to motion of body j, which originates from the frequency dependent added mass $A_{ij}(\omega)$ evaluated at $\omega \to \infty$ as in Cummins formulation (Cummins, 1962) and the frequency dependent radiation damping coefficient $B_{ij}(\omega)$, which is connected with the kernel function of the convolution integral in (6) through the inverse Fourier transformation

$$K_{ij}(t) = \frac{2}{\pi} \int_0^\infty B_{ij}(\omega) \cos(\omega t) d\omega. \tag{7}$$

The hydrodynamic information of the two real matrix functions $A_{ij}(\omega)$ and $B_{ij}(\omega)$ is contained in a time dependent matrix function $K_{ij}(t)$ and a constant matrix A_{ij}^∞. In Falnes (2002) the derivation of the Kramers–Kronig relations in hydrodynamic radiation using the principle of causality is described in more detail. With $\Gamma_i(\omega_k, \theta)$, $\Phi_i(\omega_k, \theta)$, A_{ij}^∞, $B_{ij}(\omega)$, $i, j = \{1, 2, \dots 2N\}$ and the introduced manipulations we have the main hydrodynamic coefficients, which are necessary for the EOM in the time domain. For this first study we neglect nonlinear viscous and friction effects, since the bottom of buoy is shaped like a vertically cut ring torus, reducing viscous losses. However, the time-domain formulation enables the practical correction to add those terms (Falnes, 2002).

2.2. Air chamber and turbine model

The main assumptions to model the air chamber of WEC i are an isentropic compression/expansion of the air, no heat transfer in the chamber walls and small variations in the temperature of the chamber, due to continuous in and outflow as in Henriques et al. (2017a). We restate the derivation for completeness and begin with mass balance of the chamber

$$\rho_{c_i} \dot{V}_{c_i}(t) + \dot{\rho}_{c_i} V_{c_i}(t) = -\dot{m}_{t_i}(t), \tag{8}$$

where $V_{c_i}(t)$ denotes the current chamber volume as a function of the relative position between the piston and the buoy, with the air density ρ_{c_i} and $\dot{m}_{t_i}(t)$ the mass flow through the turbine, defined positive for an exhalation. Let us define the dimensionless relative pressure inside the chamber with the atmospheric pressure p_{at}, i.e.

$$p_i^*(t) = \frac{p_i(t) - p_{at}}{p_{at}}. \tag{9}$$

The isentropic process of air compression/expansion and considering air as a perfect gas, yields

$$\rho_{c_i}(t) = \rho_{at}(p_i^*(t) + 1)^{\frac{1}{\gamma}}, \tag{10}$$

where $\gamma \approx 1.4$ denotes the specific heat ratio of air is constant under the assumptions. Taking the logarithmic derivative $L(f) := \dot{f}/f$ of (10), yields

$$\gamma \frac{\dot{\rho}_{c_i}(t)}{\rho_{c_i}(t)} = \frac{\dot{p}_i^*(t)}{p_i^*(t) + 1}. \tag{11}$$

Substituting (10) and (11) into (8) results in

$$\dot{p}_i^*(t) = -\gamma \frac{\dot{m}_{t_i}(t)}{\rho_{at} V_{c_i}(t)} \left(p_i^*(t) + 1\right)^{\frac{\gamma-1}{\gamma}} - \gamma \frac{\dot{V}_{c_i}(t)}{V_{c_i}(t)} \left(p_i^*(t) + 1\right) \tag{12}$$

Now, the time rate of change (12) of the dimensionless pressure p_i^*, which will be used as a state for the state space representation, connects the heave states of the bodies with the turbine and generator dynamics via the mass flow $\dot{m}_{t_i}(t)$. The modeling of a bi-radial turbine has been previously presented in Henriques et al. (2016b, 2017a) and Henriques et al. (2017). The time rate of change of the rotational speed Ω_i of the turbine is given by

$$\dot{\Omega}_i = \frac{1}{I_{t_i}} \left(T_{t_i} - T_{gen_i}\right) \tag{13}$$

where I_{t_i} is the moment of inertia (MOI) of the ith turbine/generator set, T_{t_i}, T_{gen_i} are instantaneous torques of the ith turbine and the generator, respectively. To identify the torque of the turbine, it is necessary to regard its performance characteristics which are presented in dimensionless form. To normalize those values, the rotational speed Ω, the turbine diameter d_t and the reference air density ρ_{in} are needed. ρ_{in} is defined under stagnation conditions at the turbine entrance and dependent on the flow direction, hence a function of the pressure difference between the chamber and the atmosphere, i.e.

$$\rho_{in_i} = \begin{cases} \rho_{at}(p_i^* + 1)^{\frac{1}{\gamma}}, & \text{if } p_i^* > 0 \quad \text{(exhalation)} \\ \rho_{at}, & \text{if } p_i^* < 0 \quad \text{(inhalation).} \end{cases} \tag{14}$$

The dimensionless pressure head can now be computed as

$$\Psi_i = \frac{p_{at} p_i^*}{\rho_{in_i} \Omega_i^2 d_t^2}, \tag{15}$$

with the diameter d_t of the turbine in the normalization factor. The dimensionless mass flow rate coefficient of a turbine is defined by

$$\Phi_i = \frac{\dot{m}_{t_i}}{\rho_{in_i} \Omega_i d_t^3}. \tag{16}$$

Finally, the dimensionless power coefficient is given by

$$\Pi_i = \frac{P_{t_i}}{\rho_{in_i} \Omega_i^3 d_t^5}. \tag{17}$$

Those three characteristic coefficients are related through the turbine efficiency as follows:

$$\eta_{t_i} = \frac{\Pi_i}{\Phi_i \Psi_i} \tag{18}$$

In Henriques et al. (2016b) Φ_i (– · –··) and η_{t_i} (– – –) are given as functions of the dimensionless pressure head Ψ_i and are illustrated in Fig. 3 together with the dimensionless power coefficient (——)
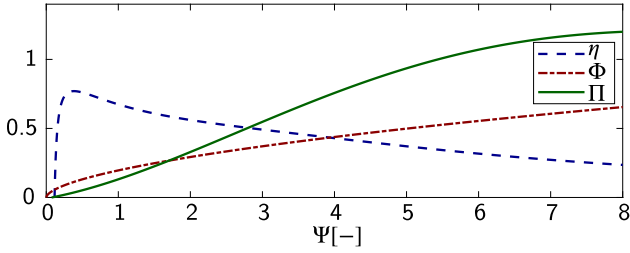
Fig. 3. Turbine characteristics as functions of the dimensionless pressure head Ψ. Namely, efficiency η, dimensionless flow rate Φ and dimensionless power coefficient Π from Henriques et al. (2017).

calculated with $\Pi = \eta \Phi \Psi$. The mass flow rate $\dot{m}_{t_i}$ can be determined from (16) and is a function of the rotational speed, which will become important regarding the controllability. As stated before, an additional high speed stop valve is installed before the biradial turbine, to realize, for example, latching, or storm protection (Henriques et al., 2017, 2016a). Assuming the HSSV can stop the entire mass flow, the mass flow rate can be stated as

$$\dot{m}_{t_i}(\Omega_i) = (1 - P_{\text{HSSV},i}) \Phi_i \rho_{\text{in}_i} \Omega_i d_t^3, \tag{19}$$

where $P_{\text{HSSV},i}$ denotes the position of the stop valve and is open for $P_{\text{HSSV},i} = 0$ and completely closed for $P_{\text{HSSV},i} = 1$, respectively. Finally, with Eqs. (17) and (18) all necessary quantities to compute the turbine torque are known, i.e.

$$T_{t_i} = \rho_{\text{in}_i} \Omega_i^2 d_t^5 \eta_{t_i} \Phi_i \Psi_i \tag{20}$$

The generator power torque T_{gen_i} is the commonly used control input to the WEC, hence the dynamics of the generator/turbine set (13) will be included in the state space representation. Additionally, the position of the HSSV provides further influence on the pressure change inside the air chamber.

2.3. State space representation

To obtain a state space model for our array of N WECs, we rewrite the equations of motion and introduce the state vector

$$x = \begin{bmatrix} x_{\text{pos}}^T & x_{\text{vel}}^T & x_{\text{press}}^T & x_{\text{kin}}^T \end{bmatrix}^T, \tag{21}$$

which consists of the vectors for heave positions x_{pos} and velocities x_{vel} of the bodies $i \ldots 2N$, the vector for the relative pressure differences inside the air chamber x_{press} of WEC $i \ldots N$ and the vector of the rotational speeds of the turbines x_{kin} of system $i \ldots N$, respectively,

$$x_{\text{pos}} = \begin{bmatrix} z_1 \\ \vdots \\ z_N \\ \vdots \\ z_{2N} \end{bmatrix} = \begin{bmatrix} x_1 \\ \vdots \\ x_N \\ \vdots \\ x_{2N} \end{bmatrix}, \quad x_{\text{vel}} = \begin{bmatrix} \dot{z}_1 \\ \vdots \\ \dot{z}_N \\ \vdots \\ \dot{z}_{2N} \end{bmatrix} = \begin{bmatrix} x_{2N+1} \\ \vdots \\ x_{3N} \\ \vdots \\ x_{4N} \end{bmatrix}, \tag{22}$$

$$x_{\text{pres}} = \begin{bmatrix} p_1^* \\ \vdots \\ p_N^* \end{bmatrix} = \begin{bmatrix} x_{4N+1} \\ \vdots \\ x_{5N} \end{bmatrix}, \quad x_{\text{kin}} = \begin{bmatrix} \Omega_1 \\ \vdots \\ \Omega_N \end{bmatrix} = \begin{bmatrix} x_{5N+1} \\ \vdots \\ x_{6N} \end{bmatrix},$$

leading to our state space representation

$$\dot{x} = \begin{bmatrix} \dot{x}_{\text{pos}} \\ \dot{x}_{\text{vel}} \\ \dot{x}_{\text{pres}} \\ \dot{x}_{\text{kin}} \end{bmatrix} = \begin{bmatrix} x_{\text{vel}} \\ (A^\infty)^{-1} \cdot \mathcal{F}(x) \\ f(x, u_{\text{HSSV}}) \\ f(x_{\text{pres}}, x_{\text{kin}}, u_{\text{gen}}) \end{bmatrix} \tag{23}$$

with

$$A^\infty = \begin{bmatrix} A_{11}^\infty & \cdots & A_{1N}^\infty & \cdots & A_{1\,2N}^\infty \\ \vdots & \ddots & \vdots & \ddots & \vdots \\ A_{N1}^\infty & \cdots & A_{NN}^\infty & \cdots & A_{N\,2N}^\infty \\ \vdots & \ddots & \vdots & \ddots & \vdots \\ A_{2N1}^\infty & \cdots & A_{2NN}^\infty & \cdots & A_{2N\,2N}^\infty \end{bmatrix} + \text{diag}\left(\begin{bmatrix} m_1 \\ \vdots \\ m_N \\ \vdots \\ m_{2N} \end{bmatrix} \right), \tag{24}$$

consisting out of the added mass components A_{ii}^∞ and the physical masses of the bodies m_i on its diagonal. This matrix originates from the radiation force component $F_i^{\text{R},\infty}$ in (6), while isolating the highest derivatives on the left hand sight of the equations of motion. $(A^\infty)^{-1}$ is responsible for an interaction between all bodies due to the dependency on the composite force, which would otherwise act on a single body, namely,

$$\mathcal{F}(x) = \begin{bmatrix} F_1^{\text{H}}(x_1) + F_1^{\text{M}}(x_1) + F_1^{\text{PTO}}(x_{4n+1}) + F_1^{\text{R}'}(x_{\text{vel}}) + F_1^{\text{Ex}} \\ \vdots \\ F_N^{\text{H}}(x_N) + F_N^{\text{M}}(x_N) + F_N^{\text{PTO}}(x_{5N}) + F_N^{\text{R}'}(x_{\text{vel}}) + F_N^{\text{Ex}} \\ \vdots \\ F_{2N}^{\text{H}}(x_{2N}) + \quad 0 \quad - F_N^{\text{PTO}}(x_{5N}) + F_{2N}^{\text{R}'}(x_{\text{vel}}) + F_{2N}^{\text{Ex}} \end{bmatrix}. \tag{25}$$

Additionally, it has to be noted that the velocity component of the radiation force $F_i^{\text{R}'}(x_{\text{vel}})$ not only does it depend on the states belonging to its own WEC system, but on the velocities of all other bodies x_{vel}, leading to further interactions between all bodies. This component has to be regarded as a separate input/output system, which will be approximated with superposition of linear time invariant state space representations of the form

$$\dot{f}_{ij}^{\text{R}'} = A_{ij}^{\text{R}'} f^{\text{R}'} + b_{ij}^{\text{R}'} z_j(t) \tag{26a}$$

$$F_{ij}^{\text{R}'} = c_{ij}^{\text{R}'} f_{ij}^{\text{R}'} + d_{ij}^{\text{R}'} z_j(t) \tag{26b}$$

using the same impulse response function as in (7). The sum over the outputs (26b) of body i affected by body j results in the desired radiation component on body i

$$F_i^{\text{R}'} = \sum_j F_{ij}^{\text{R}'}. \tag{27}$$

The system matrices can be of arbitrary dimension, but are chosen as a trade off between accuracy and computational effort due to additional states as described in the next section, along with the method used to approximate the impulse response functions. In Starrett et al. (2015) the model (26) is directly included in the EOM for a single WEC system, but due to the higher dimensions in this work we have to present the components separately. The time rate of changes

$$\dot{x}_{\text{pres},i} = f\left(z_i, z_{N+i}, \dot{z}_i, \dot{z}_{N+i}, p_i^*, \Omega_i, P_{\text{HSSV},i}\right) \tag{28}$$

and

$$\dot{x}_{\text{kin},i} = f(p_i^*, \Omega_i, T_{\text{gen},i}) \tag{29}$$

follow Eqs. (12) and (13), but are chosen to illustrate the dependencies on the other states in (23). In this model we define our inputs as the generator torque and the position of the HSSV, i.e

$$u_{\text{gen}} = \begin{bmatrix} T_{\text{gen}_1} \\ \vdots \\ T_{\text{gen}_N} \end{bmatrix}, \text{ and } u_{\text{HSSV}} = \begin{bmatrix} P_{\text{HSSV}_1} \\ \vdots \\ P_{\text{HSSV}_N} \end{bmatrix}. \tag{30}$$

3. Parameter identification

The derived model allows time domain simulations for arbitrary geometries and configurations of floating OWCs assuming the main hydrodynamic parameters are available. In this work we test the analytic equations based on three floating OWCs of the Marmok-A-5 type, developed by Oceantec Energias Marinas (Weller et al., 2017), which is illustrated in a scaled sketch in Fig. 1. The cross sections of the bodies for (2) follow from

$$S_b = \pi \left((d_b/2)^2 - (d_p/2)^2 \right) \text{ and } S_p = \pi (d_p/2)^2. \tag{31}$$

The WECs are arranged in an equilateral triangular array configuration, which is found to be optimal for multi-directional waves in de Andrés et al. (2014), with each buoy moored independently by three mooring cables building a tripod, with an angle β with the calm sea surface, as illustrated in Fig. 4. We assume β to be constant, since the offshore water depth d_w is much greater compared to the bodies motion,
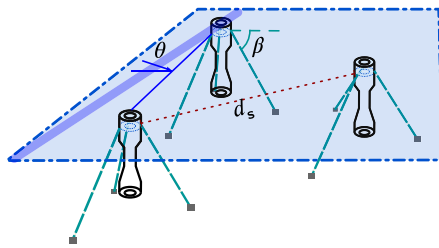
Fig. 4. Sketch of the array configuration with the plane incident wave field at angle θ, the mooring angle β and the separation distance d_s.

together with choosing the inertia and damping of the cables to be negligible, the mooring force on the buoys becomes a linear function of the vertical position greater than the calm sea surface, namely

$$F_{b_i}^{M}(t) = -3K_m \sin^2(\beta)z_{b_i}(t), \text{ for } z_{b_i}(t) > 0, \tag{32}$$

and equals zero if the body is immersed below the equilibrium point. K_m denotes the mooring stiffness of the deployed cables. Future work will incorporate more detailed non-linear mooring models and investigate the differences resulting from varying configurations, e.g inter-body moored or slack mooring. In this work we present the effects of different numerical values of K_m to illustrate the importance of the mooring force for the power generation. Instead of using one big turbine, two smaller identical biradial turbines with diameter d_t and moment of inertia I_t are used in the first full scale Marmok-A-5 prototype, with a total rated power of $30\,\mathrm{kW}$. In our example this is implemented by multiplying the instantaneous mass flow by two. To obtain the hydrodynamic coefficients necessary for the forces, we model the geometry of the array in the BEM solver ANSYS Aqwa Release 19.1 with separation d_s between each WEC system. The buoy dimensions are as illustrated in Fig. 1 and relevant to the actual parameters of the prototype. The OWC is modeled as a physical body inside the BEM modeler with a diameter $d_p^{\mathrm{BEM}} = d_p - 0.02\,\mathrm{m}$, as pictured by the red dashed box surrounding the piston in Fig. 1. Instead of using a weightless thin plate to represent the water surface inside the chamber as done in the beginning of this study, we choose a full column representation of the piston since it reduces numerical instabilities in the frequency dependent hydrodynamic coefficients, which agrees with the results of Sheng et al. (2014) and Bosma et al. (2017). Furthermore, the calculated overall mass approaches the actual one, which is of importance for the natural frequency of the piston in the time domain simulations. The incident wave angle θ ranges from $-60°$ to $60°$ in an interval of $8°$ and from $-180°$ to $180°$ in an interval of $40°$. The wave frequency is also divided into multiple ranges f_1, f_2 and f_3, to better cover the areas of interest, which require a finer resolution for low frequencies and long wave periods, respectively (See Table 1). The approximation of the infinite frequency for A_{ij}^{∞} is done with the high frequency $\omega_{\mathrm{HF}} = 100.0\,\mathrm{rad/s}$ in Aqwa 19.1.

3.1. Hydrodynamic coefficients

For a more detailed discussion of the hydrodynamic results the reader is referred to Gaebele (2018). The symmetry in the array layout reflects in the hydrodynamic characteristics of the single bodies and can be best presented on the basis of the matrix of the added mass components in (24), since the interactions are reduced to a single value. We choose to arrange our matrix so that the first N bodies are represented by the buoys, followed by the corresponding pistons in increasing enumeration. Additionally, we display all hydrodynamic coefficients with their physical units, the normalization could yield to confusion originating from the different masses of the bodies in Fig. 5. This matrix is to be read such that the body in front of a row experiences an added mass due to the acceleration of the corresponding body above a column.

Table 1
Numerical values of the simulation parameters. Quantities in lower part are exclusively used in time domain simulations.

Quantity	sym/var	Value
Spacing distance WECs	d_s	$40\,\mathrm{m}$
Water depth	d_w	$80\,\mathrm{m}$
Incident wave range 1	θ_1	$-60°:8°:60°$
Incident wave range 2	θ_2	$-180°:40°:180°$
Wave frequency range 1	f_1	$\{0.015:0.05:0.250\}[\mathrm{Hz}]$
Wave frequency range 2	f_2	$\{0.256:0.06:0.496\}[\mathrm{Hz}]$
Wave frequency range 3	f_3	$\{0.506:0.01:0.606\}[\mathrm{Hz}]$
Diameter buoy	d_b	$5.00\,\mathrm{m}$
Diameter inner tube	d_p	$2.82\,\mathrm{m}$
Piston diameter in BEM	d_p^{BEM}	$2.80\,\mathrm{m}$
Mooring angle	β	$60°$
Mooring stiffness (reg)	K_m^{reg}	$80\,\mathrm{kN/m}$
Mooring stiffness (irreg)	K_m^{irreg}	$\{60:20:140\}[\mathrm{kN/m}]$
Diameter turbine	d_t	$0.5\,\mathrm{m}$
MOI turbine	I_t	$5\,\mathrm{kg}\,\mathrm{m}^2$
Number of turbines	N_t	2

For example element $(3,6)$ expresses the added mass of $15\,998\,\mathrm{kg}$ on b_3 due to p_3. On the main diagonals we find the effects the individual body experiences based on his own motion, surrounded by the solid lines. The diagonals of the other blocks represent interactions inside the same WEC system, namely between buoy and piston. The remaining elements represent the cross coupling between spatially distinct WECs and are except for numerical variations equal in between the combinations, since the WEC are separated with the same distance from the others. Furthermore, the symmetry of the example array configuration allows us to state the hydrodynamic radiation damping coefficients $B(\omega)$ as eight wave frequency ω dependent functions instead of 36, as illustrated in Fig. 6. We continue to use the same color and line style notation as used for the added mass in Fig. 5 and the results are again given with their physical unit, since the choice for a normalization mass would distort the magnitudes while comparing buoys and pistons. The radiation damping characteristics induced by a buoy on itself $B_{b_i b_i}$ and its corresponding piston $B_{p_i b_i}$ have the largest amplitude of all the combinations and are illustrated in solid darkblue (——) and dash dotted crimson (-·-··), respectively. The subscripts $_{b_i b_i}$, $_{p_i b_i}$ indicate the equivalence for all WECs $i = \in \{1,2,3\}$. Again, we observe symmetry, namely four pairs of characteristics, each induced by a different body, acting on the two bodies from the same WEC. In other words, the buoy and the corresponding piston will always experience similar effects caused by the radiation of any specific body. It has to be noted that the radiation damping coefficients due to cross coupling change their sign multiple times over ω, best seen at the dashed blue and red line (- - -/- - -), representing the effects from a buoy on both bodies in different WECs $B_{b_i b_j}$, $B_{p_i b_j}$, $\forall i,j \in \{1,2,3\}, i \neq j$. To obtain the radiation force we would have to solve the convolution integral in (6) with the impulse response function (IRF) of $B(\omega)$ in Eq. (7). Although we are presenting eight distinct values in our case, the radiation forces are still dependent on all other body velocities, consequently we would need to solve $(2N)^2$ convolution integrals at every time step. This computational effort can be reduced by approximating $F_i^{R'}$ with the state space representation (26) after approximating the kernel function with a sum of complex exponentials, as discussed in Sheng et al. (2015), namely,

$$K_{nm}(t) = \sum_{k=1}^{N_{\mathrm{K},nm}} \alpha_{nm,k} e^{\beta_{nm,k} t}, \tag{33}$$
$$\forall n,m \in \{b_i, p_i, i \in \{1,2,3\}\},$$

since all IRFs will converge towards zero as time increases. Here $N_{\mathrm{K},nm}$ denotes the order of the approximation and thus the dimension of the intended virtual state vectors. We use Prony's method to obtain the coefficients $\alpha_{nm,k}$ and $\beta_{nm,k}$, which arise in pairs of complex conjugates
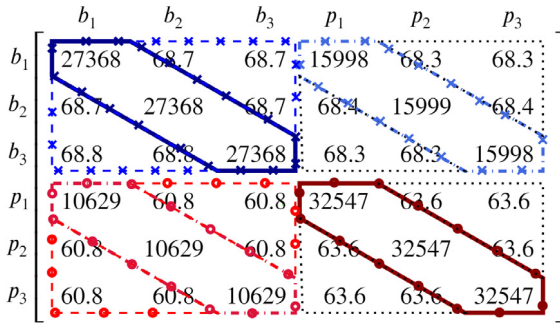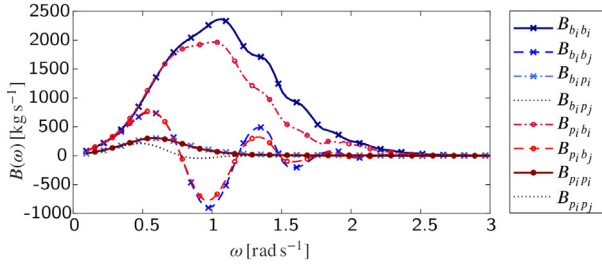
Fig. 5. Added mass with indicated array symmetry.

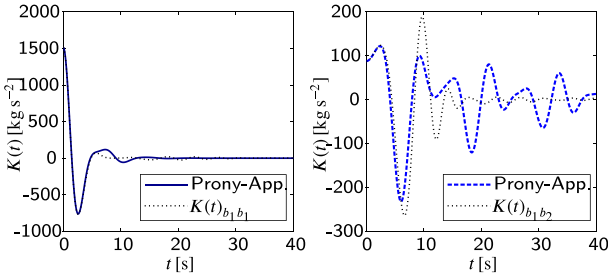**Fig. 6.** Frequency dependent radiation damping coefficients.

Fig. 7. Impulse response function of $B(\omega)$ for the radiation effects on Buoy 1 its own motion on the left (likewise representing the self damping of the other buoys). On the right: The radiation damping induced on Buoy 1 due to motion of Buoy 2, equivalent to the cross coupling between the other buoy pairs.

values. However, as the result of the sum over the pairs we receive a real value, using the relation $\exp(z) = \exp(x)(\cos y + i \sin y)$, for $z = x + iy$ if we choose an even order. For the body combinations within the same WEC system we choose an order $N_{K,nn} = 4, \forall n \in \{b_i, p_i, i \in \{1, 2, 3\}\}$. The change of the sign in $B(\omega)$ for the cross coupling combinations requires a higher order of approximation $N_{K,nm}$, i.e. $N_{K,nm} = 8, \forall n, m \in \{b_i, p_i, i \in \{1, 2, 3\}\}, n \neq m$, since the resulting IRF has its peak not at $t = 0$, but shifted in time due to the wave propagation from one WEC to another, pictured in right plot in Fig. 7 with the dotted black line ($\cdots\cdots$). We choose the example of the buoys for illustration purposes, since in this case we observe the worst fit of all body combinations, to show the limitations of this method for the cross coupling. However, the characteristic behavior is mapped with the right amplitude, illustrated in dashed blue (- - -), thus we conclude that the results are reasonable for first investigations. The causal discrete transfer functions obtained with Prony's method are converted from discrete to continuous time with the used sampling frequency of $f_{\text{samp}} = 25$ Hz and subsequently converted to the state space form (26).

The hydrodynamic excitation force coefficients and the corresponding phase coefficient complete the necessary parameters for the time domain simulation of (23). In Fig. 8 the combination of $\Gamma_{b_1}(\omega, \theta)$ and
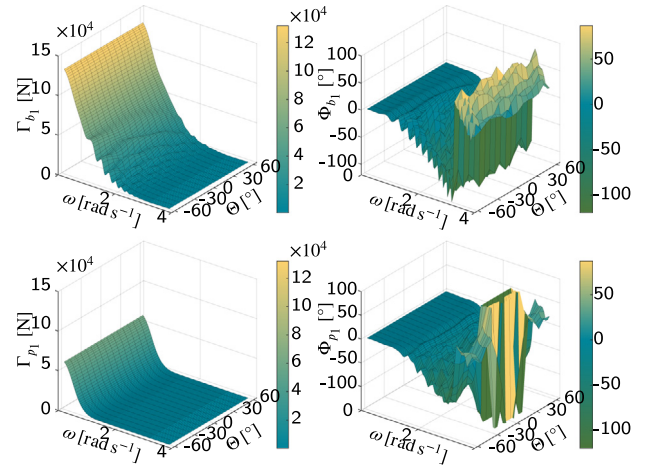

Fig. 8. Excitation force coefficients Γ_{b_1} (top), Γ_{p_1} (bottom) and their corresponding phase coefficient Φ_{b_1}, Φ_{p_1} on the right for Buoy 1 and Piston 1, respectively.

$\Phi_{b_1}(\omega, \theta)$ (top row, see Eq. (5)) and the pair of the corresponding piston $\Gamma_{p_1}(\omega, \theta)$, $\Phi_{p_1}(\omega, \theta)$ (bottom) is illustrated as an example. We observe the result for Buoy 2 if we mirror the current plot at $\theta = 0°$, due to the symmetry how the incident waves hit the array. The plot for Buoy 3 is symmetric with respect to the $\theta = 0°$ axis, due to its position on the x-axis which corresponds to the $\theta = 0°$ axis. For the pistons we find $\Gamma_{p_i}(\omega, \theta)$ to be independent of θ. However, the associated $\Phi_{p_i}(\omega, \theta)$ do vary in the manner described for the buoy. To compute $F^{\text{Ex}}(t)$ for the irregular wave case we use a significant wave height H_s and dominant period T_p to characterize a Pierson–Moskowitz (PM) wave energy spectrum with the parameters given in Falnes (2002) and define an incident wave angle θ. The PM spectrum is sampled at $N_w = 200$ wave frequencies ω_k, equally distributed over $0.2 \, \text{rad s}^{-1}$ to $2.4 \, \text{rad s}^{-1}$. During the summation over the wave frequencies $\Gamma_i(\omega_k, \theta)$ and $\Phi_i(\omega_k, \theta)$ are interpolated for constant θ and the corresponding ω_k on the basis of the illustrated coefficients for the corresponding body. Finally the shift around the random phase components ϕ_k gives us our six wave excitation force time series. Regular waves are linearly scaled with $\Gamma_i(\omega, \theta)$ to obtain the excitation force signals for regular wave scenarios.

3.2. Stabilizing control law

Henriques et al. develop an optimal feedback control law for a practical implementation in Henriques et al. (2017a), based on the maximization of the aerodynamic efficiency of a fixed OWC, equipped with the same biradial turbine, namely,

$$u_{\text{gen}} = a_{\text{gen}} \Omega^{b_{\text{gen}} - 1}. \tag{34}$$

The authors compute the time-averaged turbine output power for several sea states as a function of the rotational speed to find an optimal set of angular velocities and determine the constants a_{gen} and b_{gen} with a least-squares fitting. In this work we set the coefficients to $a_{\text{gen}} = 0.0001$ and $b_{\text{gen}} = 3.6$ following Henriques et al. (2017a) for the same order and we cannot guarantee optimal values for the simulated sea state. However, they are suitable to achieve realistic results for initial evaluation. The exponent of the rotational speed in Eq. (34) is chosen so that the power of an ideal generator is given by

$$P_{\text{gen}} = a_{\text{gen}} \Omega^{b_{\text{gen}}}. \tag{35}$$

In this baseline model an ideal generator is assumed by means of the electromagnetic torque applied to the turbine will directly result in an energy conversion. For future work, several generator types will be incorporated into the simulation environment to assess performance using practical devices.
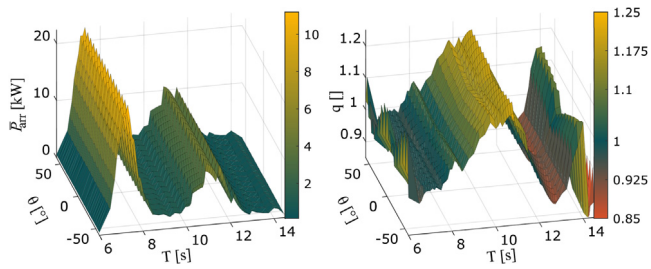
Fig. 9. Averaged generated power off the array $\bar{P}_{arr}$ in regular waves (left) and the corresponding array interaction factor q (right).

4. Time domain simulation

Numerical simulations of the derived state space model (23) are conducted with MATLAB® Simulink in the time domain taking into account the nonlinear effects of a compressible fluid in the air chamber and the specific turbine model.

4.1. Regular waves

The first results of the generated power of the three WECs and the corresponding array interaction factor

$$q(\theta, T) = \frac{\bar{P}_{arr}}{3 \bar{P}_{single}} \tag{36}$$

presented in Fig. 9 are obtained using regular Stokes waves of 3rd order (Stokes, 1847) with wave height of $H_s = 1\,m$ from varying incident wave angles θ and varying wave periods T. The concept of the interaction factor is widely used in the literature on WEC arrays and restated in terms of the averaged power of the array $\bar{P}_{arr}(\theta, T)$ and the averaged power of a single isolated devise $\bar{P}_{single}(\theta, T)$ in the same wave scenario. After sufficiently long simulation time the dynamics reach an asymptotic behavior for every θ, T combination and the last three entire periods of the transient oscillation of each WEC are used to compute $\bar{P}_{arr}(\theta, T)$ which is illustrated in Fig. 9 on the left. To reduce the simulation time around five times, we use the terminal state of the previous simulation run as initial condition for the next simulation run with varied incident wave angle of $\Delta\theta = 4°$, thus reach the transient motion in less time. We observe two peaks in the generated power for a varying wave period, where the peak at the lower period $T = 7.3\,s$ results from a decreased oscillation amplitude of the water column and an increased amplitude of the buoy, respectively. The opposite is the case for the second peak around $T = 11.2\,s$, where the amplitude of the pistons motions is higher compared to the buoy. In both cases the relative motion between the two bodies is locally maximized, which is typical for floating two body heaving systems, likewise observed for linear frequency domain simulations in Gomes et al. (2012). The energetic long periodic waves $T \geq 14\,s$ result in a motion of both buoy and piston following the water surface elevation, hence the relative motion in the floating OWC tends towards zero, likewise the generated power. For short wave periods the excitation force converges towards zero (compare Γ_i in Fig. 8), resulting in minimal body motion, which also does not yield power generation for $T \leq 6\,s$. Consequently, the peaks in the q-factor at the boundaries of the wave period range are not of importance, since the significance is lost when dividing a numerically small number by a small number in Eq. (36). The area of the highest $q \geq 1.15$ around $T \in \{9.25\,s \dots 11.2\,s\}$ implies that the power generation inside the array is increased due to an increase of the pistons' motion, which can be explained by the hydrodynamic interactions affecting the water columns more relative to the buoys.
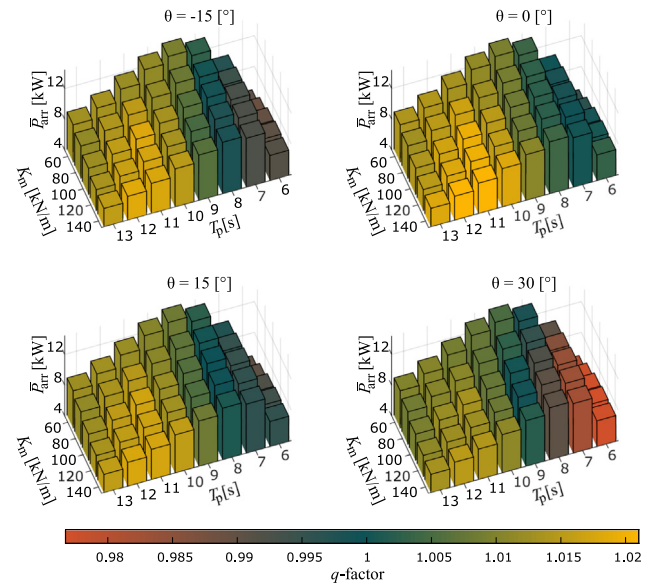

Fig. 10. Averaged generated power off the array $\bar{P}_{arr}$ in irregular waves versus significant wave periods T_s and mooring stiffness K_m for varied incident wave angles θ in each subplot. The corresponding array interaction factor q is represented by the bars' color.

4.2. Irregular waves

For more realistic sea states we choose a wave which is irregular in the amplitude, but otherwise propagating as a plane wave, to be able to distinguish possible interaction effects from the approximation of the diffraction and radiation problem inside the array with the evaluation of the generated power compared to the power generated for the same wave in an isolated device and in terms of differences in the motion of the bodies. A wave characterized with the PM spectrum based on $H_s = 2\,m$ and different peak periods $T_p = \{6\,s, 7\,s, \dots 13\,s\}$ is the foundation for the excitation force. The incident wave angle is chosen to be $\theta = \{-15°, 0°, 15°, 30°\}$. A further parameter we vary is the mooring stiffness $K_m = \{60\,kN/m, 80\,kN/m \dots, 140\,kN/m\}$ to investigate its relevance to the output. The generated power $\bar{P}_{arr}$ is averaged over the time window between 60 and 660 s, since we start the simulation from the initial equilibrium and wait for steady-state motion. In Fig. 10 $\bar{P}_{arr}$ is illustrated versus K_m and T_p in each subplot for a different θ. It has to be noted that the subplots are rotated to enable visualization of each bar, but consequently the abscissa and ordinate are decreasing. Furthermore, although unity remains the same color as in Fig. 9, the colormap has different limits, enabling the identification of the maximum and minimum simulated q-factor for the irregular waves scenarios in terms of the color of the bars. Due to symmetry the scenarios for $\theta = 15°$ and $\theta = -15°$ are equal, ignoring minor numerical variations. Except for $T_p = 6\,s$ (decrease in excitation, compared to regular waves in Fig. 9) a decreasing K_m yields an increase in $\bar{P}_{arr}$, since the buoys are less restricted in motion. For the irregular waves scenarios we do not observe the two peaks in power as in the regular waves case in Fig. 9 over the peak wave period but a more evenly distributed power generation. Generally, $q > 1$ for $T_p > 9\,s$, while the highest interaction factor is achieved for $\theta = 0°$, $T_p = 12\,s$ and $K_m = 140\,kN/m$. However, the difference in q is small compared to the regular wave scenario.

Information about the time evolution of the states can be characterized by a single simulation run. We set $H_s = 2\,m$ and $T_p = 10\,s$ to emulate a wave which is typically observed in the US Pacific Northwest (Lenee-Bluhm et al., 2011). The mooring stiffness is set to $K_m = 80\,kN/m$, equal to the regular wave scenario and an incident wave angle $\theta = 30°$ results in different arrival times at each WEC, such
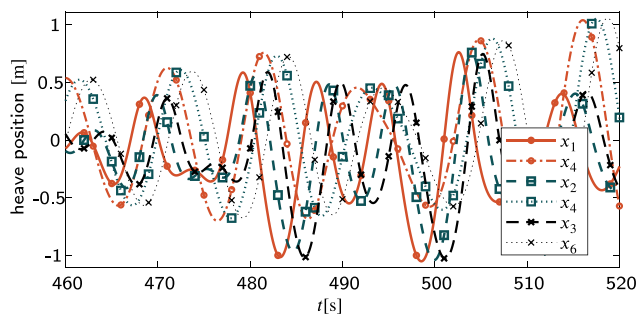
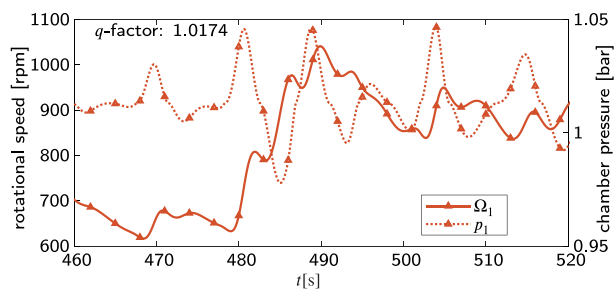**Fig. 11.** Heave positions of all the bodies inside the array.

Fig. 12. Rotational speed and chamber pressure of WEC 1.

that the peaks of the bodies positions are shifted in time. In Fig. 11 we show the heave positions between 460 and 520 s, since characteristic effects can be observed during this time window. The solid and dashed lines represent the positions of the buoys while the dash-dotted and dotted lines of the same color and marker represents the corresponding piston. In the sketch of the array in Fig. 4 the first buoy with heave position x_1 is the furthermost one, thus it is reached first by the wave, since $\theta > 0$ given in orange (———) with circled marker followed by the second WEC system illustrated with the blue green dashed line (- - -) with square markers. The black dashed plot (- - -) with cross markers shows the motion of the third buoy, which is always reached last for the used θ. The differences between a local extrema for different WECs are hard to notice with the naked eye, but e.g. the peak of x_1 before $t =$ 490 s is 0.025 m higher than those of the two other buoys. Generally it can be observed that the motion of the piston is shifted from the buoys motion therefore a varying relative motion inside the two-body heaving system results, leading to the pressure change in the air chamber. This pressure p_1 is illustrated for the first WEC with the same orange in Fig. 12 as dotted line (· · · · ·) with triangle markers and oscillates about the atmospheric pressure. A turbine is accelerated for an inflow as well as an outflow, thus the high frequency oscillation on the rotational speed graph in solid orange (———) has half of the wave and bodies period. We notice high variations in Ω, for example from 480 to 490 s since it follows the peaks in the chamber pressure, reflecting the varying oscillation amplitudes of our WEC systems. During this period WEC 1 picks up on motion amplitude in addition to a higher difference to the change in the relative position with the corresponding OWC. This behavior results in an unsteady power output, because in this case we do not control the rotational speed based on any other information apart from itself.

5. Discussion

As illustrated by the motions in Fig. 11 the differences between distinct systems are small compared to the total range of motion in irregular waves. Additionally, in more realistic sea states the computed interaction factor q only varies by $\approx 5\%$. This implies that the radiation

and diffraction problem inside the investigated array has no greater impact for this specific example, which can be explained with the geometry of the Marmok-A-5 devices. The ratio of the diameter d_b to the draft is small, about 0.14, which is connected to weak radiation properties. Furthermore, the separation distance compared to diameter the has to be mentioned. With $d_s = 8d_b$ the buoys are far apart. However, d_s is chosen this way to guarantee that maintenance ships can navigate between the WEC devices without colliding with them, since the roll and pitch motion is not yet evaluated. In Appendix an outlook to include other degrees of freedom and the phenomenon of parametric resonance is given. The simulation results herein presented, after inspecting the hydrodynamic coefficients of our case study, appear to be reasonable. The added mass and especially its inverse has the largest entries on its diagonal, which implies a high dependency on its own component in the composite force for every WEC body. Additionally, the magnitudes of the IRFs are small compared to the mass dimensions of the bodies, with the cross coupling terms being even smaller by at least an order of magnitude. The diffraction inside the array, reflected by the differences between the excitation force coefficients, is as well marginal and the excitation is much more related to the wave frequency compared to anything else. Nevertheless, the simulation results in regular wave suggest that the employment of this specific floating OWCs in an array can widen the range of regular waves frequencies desirable for energy conversion, which agrees with $q > 1$ for $T_p > 9\,\text{s}$ for the irregular case. However, we also observe q below unity for some wave periods, implying destructive interference, which suggest future investigations of different array configurations to be able to optimize the layout and separation for different wave climates for the floating OWCs and compare the results to existing approaches on different two-body heaving systems (de Andrés et al., 2014) or fixed OWCs (Sharp et al., 2017, 2018). The differences resulting from varying incident wave angle θ are again marginal due to the symmetry of the array, but cannot be generalized for non-symmetric configurations. Subsequent work will also consider the effects of viscous drag forces, to obtain a more practical representation. The PTO and the air chamber model are highly nonlinear and the strong changes in simulated rotational speed in Fig. 12 suggest further investigations of a sliding mode controller, which with its discontinuous nature should perform well in maintaining a constant Ω. This rotational speed will be set to a value resulting in an improved efficiency of the turbine. To this date the authors do not know of any studies addressing optimal control of floating OWC parks with nonlinear PTO. Future research will aim for semi-global control of sub-array off several devices, followed by decentralized supervising control for entire WEC parks. Large arrays of WEC devices will need different methodologies to model the hydrodynamic interactions. This work can serve as basis for the comparison of results, when methods to derive the diffraction and radiation capabilities based on the hydrodynamics of an single device, like McNatt et al. (2015) are adapted to floating OWCs.

6. Conclusion

We derived a methodology to efficiently model full scale arrays of floating OWCs taking hydrodynamic interactions between all distinct bodies into account without making simplification in the devices geometries as well as connected them to a nonlinear air chamber/turbine model. The approach is neither limited to an symmetric array nor to identical devices but to the availability of the linear hydrodynamic coefficients simulated for the entire configuration. The case study of the Marmok-A-5 is used, since it is one kind of device that has actually been deployed and tested in the ocean. We found that for the assumed separation between the single devices, we could neglect the cross coupling between the WECs in irregular waves but not in regular waves. However, different mooring configurations or further insights in the real world constraints of the array placement could justify a smaller separation and consequently higher hydrodynamic interactions.

Nevertheless, the analytic model can be used to design more advanced control strategies like nonlinear sliding mode control to maintain a constant rotational speed, or methods aiming to optimize the power generation, for example by means of smoothing the power output. The next step in our research will consider semi-global control approaches for sub-arrays, followed by supervisory control for entire WEC parks.

Acknowledgment

Appendix. Multiple degrees of freedom

Increasing the number of the degrees of freedom (DoF) in the presented coupled model can be achieved by expanding the system equations, namely by adding more spatial states to the sub state vectors x_{pos} and consequently to x_{vel}. The procedure is illustrated with help of the roll angle ϕ as an example. The time derivative of the bodies velocities from (23) evolves to

$$\dot{x}_{\text{vel}} = \begin{bmatrix} \ddot{z} \\ \ddot{\phi} \end{bmatrix} = \begin{bmatrix} (\boldsymbol{A}^{\infty})^{-1} & \left(\boldsymbol{A}_{z\phi}^{\infty}\right)^{-1} \\ \left(\boldsymbol{A}_{\phi z}^{\infty}\right)^{-1} & \left(\boldsymbol{A}_{\phi\phi}^{\infty}\right)^{-1} \end{bmatrix} \begin{bmatrix} \boldsymbol{\mathcal{F}}(\boldsymbol{x}) \\ \boldsymbol{\mathcal{T}}_{\phi}(\boldsymbol{x}) \end{bmatrix}. \tag{37}$$

Here $\left(\boldsymbol{A}_{ij}^{\infty}\right)^{-1} \in \mathbb{R}^{2N \times 2N}$ is defined in the same manner as $(\boldsymbol{A}^{\infty})^{-1}$ is defined in section 2.3 and the subscripts denote the interaction from the DoF j to i. The accumulated torques on the roll axis are represented by $\boldsymbol{\mathcal{T}}_{\phi}(\boldsymbol{x})$ and would not act on the pistons. The second part of radiation problem (Eq. (6)) can be obtained as described in Section 3.1. However, the necessary interaction terms increase quadratically with the number of DoFs N_{DoF}, namely $(2NN_{\text{DoF}})^2$. Therefore a trade off between accuracy and computational effort has to be obtained by neglecting the non-significant interactions. The coupling of at least two DoFs enables the phenomenon of parametric resonance to occur, under the condition that the incident wave frequency is approximately twice the pitch or roll natural frequency (Rodríguez and Neves, 2016; Rho et al., 2005). This dynamic instability is commonly found in spar type oscillating water columns extracting energy in heave direction (Gomes et al., 2017). The state equations are further coupled by the metacentric height (GM) in $\boldsymbol{\mathcal{T}}_{\phi}(\boldsymbol{x})$, which varies with instantaneous heave position of the device, directly affecting the center of buoyancy of the spar. If the GM becomes negative, the motion becomes unstable, decreasing the extracted power, since kinetic energy is transferred from the heave mode to the pitch mode (Rho et al., 2005). Those phenomena have to noted, if more detailed studies of the motion of WEC farms are desired.

References

Aderinto, T., Li, H., 2018. Ocean wave energy converters: Status and challenges. Energies 11, 1250. http://dx.doi.org/10.3390/en11051250.

de Andrés, A., Guanche, R., Meneses, L., Vidal, C., Losada, I., 2014. Factors that influence array layout on wave energy farms. Ocean Eng. 82, 32–41. http://dx.doi.org/10.1016/j.oceaneng.2014.02.027.

Andrews, J., Jelley, N., 2017. Energy Science - Principles, Technologies, and Impacts, third ed. Oxford University Press.

Bacelli, G., Ringwood, J.V., 2015. Numerical optimal control of wave energy converters. IEEE Trans. Sustain. Energy 6 (2), 294–302. http://dx.doi.org/10.1109/TSTE.2014.2371536.

Bosma, B., Brekken, T.K.A., Lomonaco, P., Mckee, A., Paasch, B., Batten, B., Physical model testing and system identification of a cylindrical OWC device. In: 12th European Wave and Tidal Energy Conference (EWTEC), Aug 2017. pp. 910: 1–10.

Budal, K., 1977. Theory for absorption of wave power by a system of interacting bodies.. J. Ship Res. 21, 248–253.

Chowdhury, S., Nader, J.-R., Madrigal Sanchez, A., Fleming, A., Winship, B., Illesinghe, S., Toffoli, A., Babanin, A., Penesis, I., Manasseh, R., 2015. A review of hydrodynamic investigations into arrays of ocean wave energy converters. https://arxiv.org/ftp/arxiv/papers/1508/1508.00866.pdf.

Cummins, W., 1962. The impulse response function and ship motions. In: Symposium on Ship Theory at the Institut für Schiffbau der Universität Hamburg.

Falcão, A.F.d.O., 2002. Wave-power absorption by a periodic linear array of oscillating water columns. Ocean Eng. 29, 1163–1186. http://dx.doi.org/10.1016/S0029-8018(01)00076-2.

Falcão, A.F.d.O., 2010. Wave energy utilization: A review of the technologies. Renew. Sustain. Energy Rev. 14 (3), 899–918. http://dx.doi.org/10.1016/j.rser.2009.11.003.

Falcão, A.F.d.O., Henriques, J.C.C., 2016. Oscillating-water-column wave energy converters and air turbines: A review. Renew. Energy 85, 1391–1424. http://dx.doi.org/10.1016/j.renene.2015.07.086.

Falnes, J., 2002. Ocean waves and oscillating systems. Cambridge University Press.

Forehand, D.I.M., Kiprakis, A.E., Nambiar, A.J., Wallace, A.R., 2016. A fully coupled wave-to-wire model of an array of wave energy converters. IEEE Trans. Sustain. Energy 7 (1), 118–128. http://dx.doi.org/10.1109/TSTE.2015.2476960.

Gaebele, D.T., 2018. Modelling of an array of floating oscillating water column wave energy converts with full hydrodynamic coupling and nonlinear power take off dynamics. (Master's thesis). University of Stuttgart, Institute for System Dynamics, Stuttgart, Germany.

Gomes, R.P.F., Henriques, J.C.C., Gato, L.M.C., Falcão, A.F.d.O., 2012. Hydrodynamic optimization of an axisymmetric floating oscillating water column for wave energy conversion. Renew. Energy 44, 328–339. http://dx.doi.org/10.1016/j.renene.2012.01.105.

Gomes, R.P.F., Malvar Ferreira, J.D.C., Ribeiro e Silva, S., Henriques, J.C.C., Gato, L.M.C., 2017. An experimental study on the reduction of the dynamic instability in the oscillating water column spar buoy.

Henriques, J.C.C., Gato, L.M.C., Falcão, A.F.d.O., Robles, E., Faÿ, F.X., 2016a. Latching control of a floating oscillating-water-column wave energy converter. Renew. Energy 90, 229–241. http://dx.doi.org/10.1016/j.renene.2015.12.065.

Henriques, J.C.C., Gomes, R.P.F., Gato, L.M.C., Falcão, A.F.d.O., Robles, E., Ceballos, S., 2016b. Testing and control of a power take-off system for an oscillating-water-column wave energy converter. Renew. Energy 85, 714–724. http://dx.doi.org/10.1016/j.renene.2015.07.015.

Henriques, J.C.C., Lemos, J.M., Gato, L.M.C., Falcão, A.F.d.O., Portillo, J.C.C., 2017b. Latching and peak-power control of an oscillating water column based on a discontinuous Galerkin method. In: 12th European Wave and Tidal Energy Conference (EWTEC), Aug 2017. pp. 703: 1–9.

Henriques, J.C.C., Sheng, W., Falcão, A.F.d.O., Gato, L.M.C., 2017a. A comparison of biradial and wells air turbines on the mutriku breakwater OWC wave power plant. In: ASME 2017 36th International Conference on Ocean, Offshore and Arctic Engineering Volume 10: Ocean Renewable Energy. http://dx.doi.org/10.1115/OMAE2017-62651.

Lenee-Bluhm, P., Paasch, R., özkan Haller, H.T., 2011. Characterizing the wave energy resource of the US pacific northwest. Renew. Energy 36 (8), 2106–2119. http://dx.doi.org/10.1016/j.renene.2011.01.016.

McNatt, J.C., Venugopal, V., Forehand, D., 2015. A novel method for deriving the diffraction transfer matrix and its application to multi-body interactions in water waves. Ocean Eng. 94, 173–185. http://dx.doi.org/10.1016/j.oceaneng.2014.11.029.

Nader, J.-R., Fleming, A., Macfarlane, G., Penesis, I., Manasseh, R., 2017. Novel experimental modelling of the hydrodynamic interactions of arrays of wave energy converters. Int. J. Mar. Energy 20, 109–124. http://dx.doi.org/10.1016/j.ijome.2017.11.003.

Nader, J.-R., Zhu, S.-P., Cooper, P., 2014. Hydrodynamic and energetic properties of a finite array of fixed oscillating water column wave energy converters. Ocean Eng. 88, 131–148. http://dx.doi.org/10.1016/j.oceaneng.2014.06.022.

Nambiar, A.J., Forehand, D.I.M., Kramer, M.M., Hansen, R.H., Ingram, D.M., 2015. Effects of hydrodynamic interactions and control within a point absorber array on electrical output. Int. J. Mar. Energy 9, 20–40. http://dx.doi.org/10.1016/j.ijome.2014.11.002.

Rho, J.B., Choi, H.S., Shin, H.S., Park, I.K., 2005. A study on mathieu-type instability of conventional spar platform in regular waves. Int. J. Offshore Polar Eng. 15 (2), 104–108.

Rodríguez, C.A., Neves, M.A., 2016. Investigation on parametrically excited motions of spar platforms in waves. Fluid Mech. Appl. 119, 291–305. http://dx.doi.org/10.1007/978-3-030-00516-0_17.

Rusu, L., Onea, F., 2017. The performance of some state-of-the-art wave energy converters in locations with the worldwide highest wave power. Renew. Sustain. Energy Rev. 75, 1348–1362. http://dx.doi.org/10.1016/j.rser.2016.11.123.

Sabuncu, T., Calisal, S., 1981. Hydrodynamic coefficients for vertical circular cylinders at finite depth. Ocean Eng. 8 (1), 25–63. http://dx.doi.org/10.1016/0029-8018(81)90004-4.

Sharp, C., DuPont, B., Bosma, B., Lomonaco, P., Batten, B., 2017. Array optimization of fixed oscillating water columns for active device control. In: 12th European Wave and Tidal Energy Conference (EWTEC), Aug 2017.

Sharp, C., DuPont, B., Bosma, B., Lomonaco, P., Batten, B., 2018. Array design and device damping assignment of fixed oscillating water columns. In: 6th Annual Marine Energy Technology Symposium (METS2018), May 2018.

Sheng, W., Alcorn, R., Lewis, T., 2014. Assessment of primary energy conversions of oscillating water columns. 1. Hydrodynamic analysis. J. Renew. Sustain. Energy 6, 053113. http://dx.doi.org/10.1063/1.4896850.

Sheng, W., Alcorn, R., Lewis, A., 2015. A new method for radiation forces for floating platforms in waves. Ocean Eng. 105, 43–53. http://dx.doi.org/10.1016/j.oceaneng.2015.06.023.

Starrett, M., So, R., Brekken, T.K.A., McCall, A., 2015. Development of a state space model for wave energy conversion systems. In: 2015 IEEE Power Energy Society General Meeting. pp. 1–5. http://dx.doi.org/10.1109/PESGM.2015.7285998.

Stokes, G.G., 1847. On the theory of oscillatory waves. Trans. Cambr. Philos. Soc. 8, 441–455.

Weller, S., Parish, D., Gordelier, T., A Garcia, E., Goodwin, P., Tornroos, D., Johanning, L., De Miguel Para, B., 2017. Open sea OWC motions and mooring loads monitoring at BiMEP. In: 12th European Wave and Tidal Energy Conference (EWTEC), Aug 2017. http://hdl.handle.net/10871/28593.